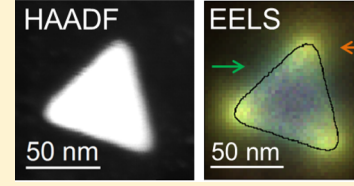


Unveiling Nanometer Scale Extinction and Scattering Phenomena through Combined Electron Energy Loss Spectroscopy and **Cathodoluminescence Measurements**

Arthur Losquin,^{†,‡} Luiz F. Zagonel,^{†,§} Viktor Myroshnychenko,^{∥,⊥} Benito Rodríguez-González,[¶] Marcel Tencé,[†] Leonardo Scarabelli, Jens Förstner, Luis M. Liz-Marzán, H.O. F. Javier García de Abajo, Odile Stéphan, and Mathieu Kociak*, de Abajo, Volume Stéphan, de Abajo, Abajo, de Abajo, Abajo,

Supporting Information

ABSTRACT: Plasmon modes of the exact same individual gold nanoprisms are investigated through combined nanometer-resolved electron energy-loss spectroscopy (EELS) and cathodoluminescence (CL) measurements. We show that CL only probes the radiative modes, in contrast to EELS, which additionally reveals dark modes. The combination of both techniques on the same particles thus provides complementary







information and also demonstrates that although the radiative modes give rise to very similar spatial distributions when probed by EELS or CL, their resonant energies appear to be different. We trace this phenomenon back to plasmon dissipation, which affects in different ways the plasmon signatures probed by these techniques. Our experiments are in agreement with electromagnetic numerical simulations and can be further interpreted within the framework of a quasistatic analytical model. We therefore demonstrate that CL and EELS are closely related to optical scattering and extinction, respectively, with the addition of nanometer spatial resolution.

KEYWORDS: nanooptics, plasmonics, electron energy loss spectroscopy, cathodoluminescence, bright and dark modes, light scattering

he last two decades have witnessed impressive advances in the synthesis of a vast range of nanoobjects with new and intriguing optical properties that are strongly dependent on their exact shape, size, composition, and local environment, opening new possibilities within the active field of nanooptics. Understandably, advances in this field have been largely fuelled by the availability of techniques that address optical properties at the nanometer scale, as well as new theoretical and simulation tools. Previously unexplored fundamental issues are raised, and in particular the classical optical concepts of extinction, absorption, and scattering are no longer sufficient to describe optical phenomena at the nanoscale. Instead, the spatial and spectral distributions of photonic eigenmodes have been recognized to play an important role when interpreting experimental outputs delivered by numerous near-field techniques. 1-8 Likewise, concepts such as the local density of optical states (LDOS)9 or alternative descriptions in terms of modal decompositions¹⁰ have become relevant for understanding nanoscale-resolved experiments, including scanning near-field optical microscopy, 11,12 thermal radiation scanning tunnelling microscopy, 13 electron energy-loss spectroscopy (EELS), $^{12,14-20}$ and cathodoluminescence (CL). 16,17,21,22 Nevertheless, the physics embodied in optical extinction, absorption, and scattering phenomena should hold, to some extent, at the nanometer scale. In other words, we still need to understand how a nanostructure absorbs and scatters electromagnetic waves at subwavelength scales. An experimental and

Received: November 14, 2014 Revised: January 4, 2015 Published: January 20, 2015



[†]Laboratoire de Physique des Solides CNRS/UMR8502, Bâtiment 510, University Paris-Sud, Orsay 91405, France

[‡]Department of Physics, Lund University, P.O. Box 118, SE-221 00 Lund, Sweden

[§]Instituto de Física Gleb Wataghin, Universidade Estadual de Campinas, Unicamp, Campinas, São Paulo 13083-970, Brazil

Instituto de Química-Física - CSIC, Serrano 119, 28006 Madrid, Spain

 $^{^{\}perp}$ Institute of Electrical Engineering, University of Paderborn,Warburger Strasse 100, D-33098 Paderborn, Germany

[¶]Departamento de Química Física, Universidade de Vigo, 36310 Vigo, Spain

[#]Bionanoplasmonics Laboratory, CIC biomaGUNE, Paseo de Miramón 182, 20009 Donostia-San Sebastián, Spain

 $^{^{}abla}$ ICFO-Institut de Ciencies Fotoniques, Mediterranean Technology Park, 08860 Castelldefels (Barcelona), Spain

^OIkerbasque, Basque Foundation for Science, 48013 Bilbao, Spain

[◆]ICREA-Institució Catalana de Recerca i Estudis Avançats, Passeig Lluís Companys, 23, 08010 Barcelona, Spain

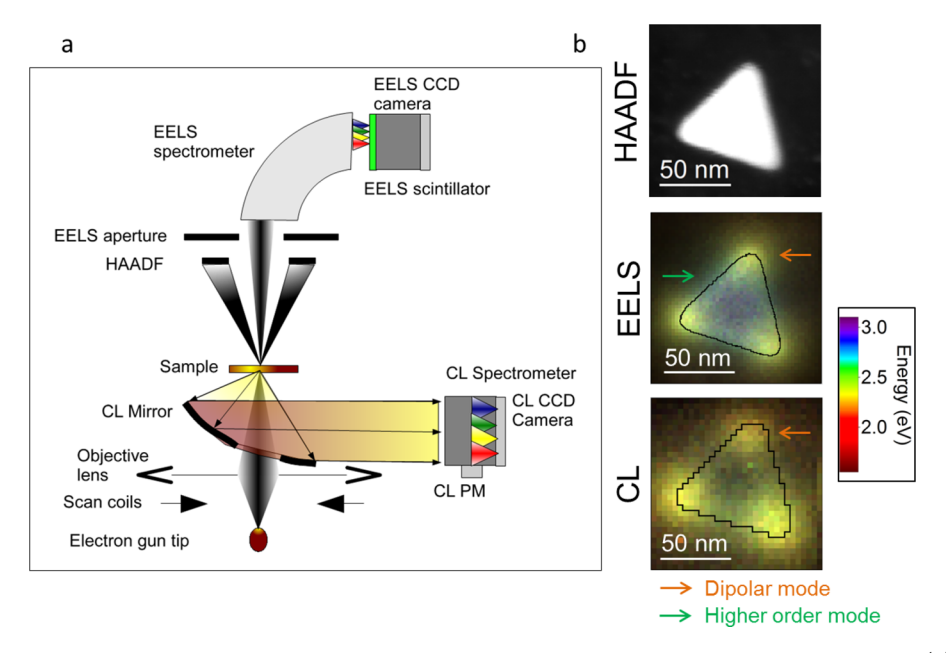


Figure 1. (a) Scheme of a scanning transmission electron microscope equipped with EELS and CL detection systems. (b) Combined HAADF imaging (top), EELS (middle), and CL (bottom) spatially resolved data sets. Total acquisition times are 157 s for CL and 16 s for EELS. In the case of EELS, the spectra are first deconvolved and normalized. The CL and EELS images are generated by coloring each filtered maps of the data sets according to its energy, weighing each pixel of the maps by its intensity and summing all the resulting images. This simplified representation of the EELS and CL data sets straightforwardly shows that the EELS data exhibit both dipolar and higher order modes, whereas the CL data exhibit mainly the dipolar mode. The black lines superimposed on the maps indicate the prism shape as obtained from the HAADF image.

theoretical framework reconciling both approaches, thus, is necessary.

EELS and CL, which have proved to be outstanding tools for studying surface plasmons (SP) with superior spatial resolution even in the most complex systems,²³ are suitable candidates to address these issues. 24 In these techniques, a fast electron (typically traveling at half the speed of light) is focused onto or close to the nanostructure of interest. The electron is capable of transferring energy to the nanostructure via electromagnetic interaction.²⁵ This amount of energy is measured by analyzing the stopping experienced by the electron in EELS or by detecting the emitted light resulting from the interaction in CL. Therefore, it is basically the electromagnetic nature of the electron-sample interaction that allows us to explore the optical response of the nanostructure. In particular, CL relates to the ability of the nanostructure to scatter the evanescent electromagnetic field carried by the electron into the far field, whereas EELS probes the sum of radiative losses (i.e., CL) plus energy transfers that are inelastically absorbed by the materials involved. This close relationship between fast-electron-based spectroscopies and optical properties has been emphasized in qualitative interpretations of EELS and CL experiments in terms of either absorption, extinction, or scattering.²⁶⁻³⁰ However, the apparent connection between EELS and extinction on the one hand and CL and scattering on the other hand, which is also suggested by modal decomposition analyses in the case of spheres, ^{16,24} has not been addressed theoretically in a general case. From the experimental viewpoint, we remark that combined EELS/CL experiments on the same nanoobject and in the same environment are still missing, precluding a fair, exact comparison of both techniques. Thus, we still lack a direct proof of the possibility of measuring optical extinction and scattering at the nanometer scale, as well as a clear evidence of the intimate relationship between

traditional optics-based measurements and subwavelength-resolved electron-beam spectroscopies.

In this article, we present experimental and theoretical evidence that spatially resolved EELS and CL experiments performed on the same individual metallic nanoparticles allow us to directly disentangle radiative and nonradiative modes on an individual particle basis. We also show that EELS and CL are closely connected to optical extinction and scattering phenomena at the nanometer scale. By collecting nanometerresolved EELS and CL spectra from the same individual small gold triangular nanoprisms, we first demonstrate that only the dipolar mode is measured by both techniques, whereas the higher order modes are only accessible through EELS. This is a clear experimental signature of the inability of CL to detect nonradiative modes, in contrast to EELS. We further demonstrate that dipolar SP modes, as measured by both techniques, may appear to have different resonance energies although they give rise to similar intensity spatial distributions. Simulations clearly show that such spectral differences between EELS and CL are also present in light extinction and scattering. As a consequence, the main spectral differences between extinction and scattering observed when examining individual nanoparticles as a whole via far-field spectroscopies are qualitatively maintained upon nanoscale inspection within individual nanoparticles through EELS and CL. We formulate modal decompositions in the quasistatic limit for CL, as well as for optical extinction and scattering, and compare them to a previously derived formula for EELS. This helps us to understand in simple terms the role of dissipation that we report in both experiments and simulations, which affects extinction and scattering phenomena in distinct ways.

Gold triangular nanoprisms are synthesized using a seed-mediated growth in aqueous media; ^{31,32} briefly, a small amount of iodide ions is exploited to guide the two-step growth of gold seeds stabilized by cetyltrymethilammonium chloride toward

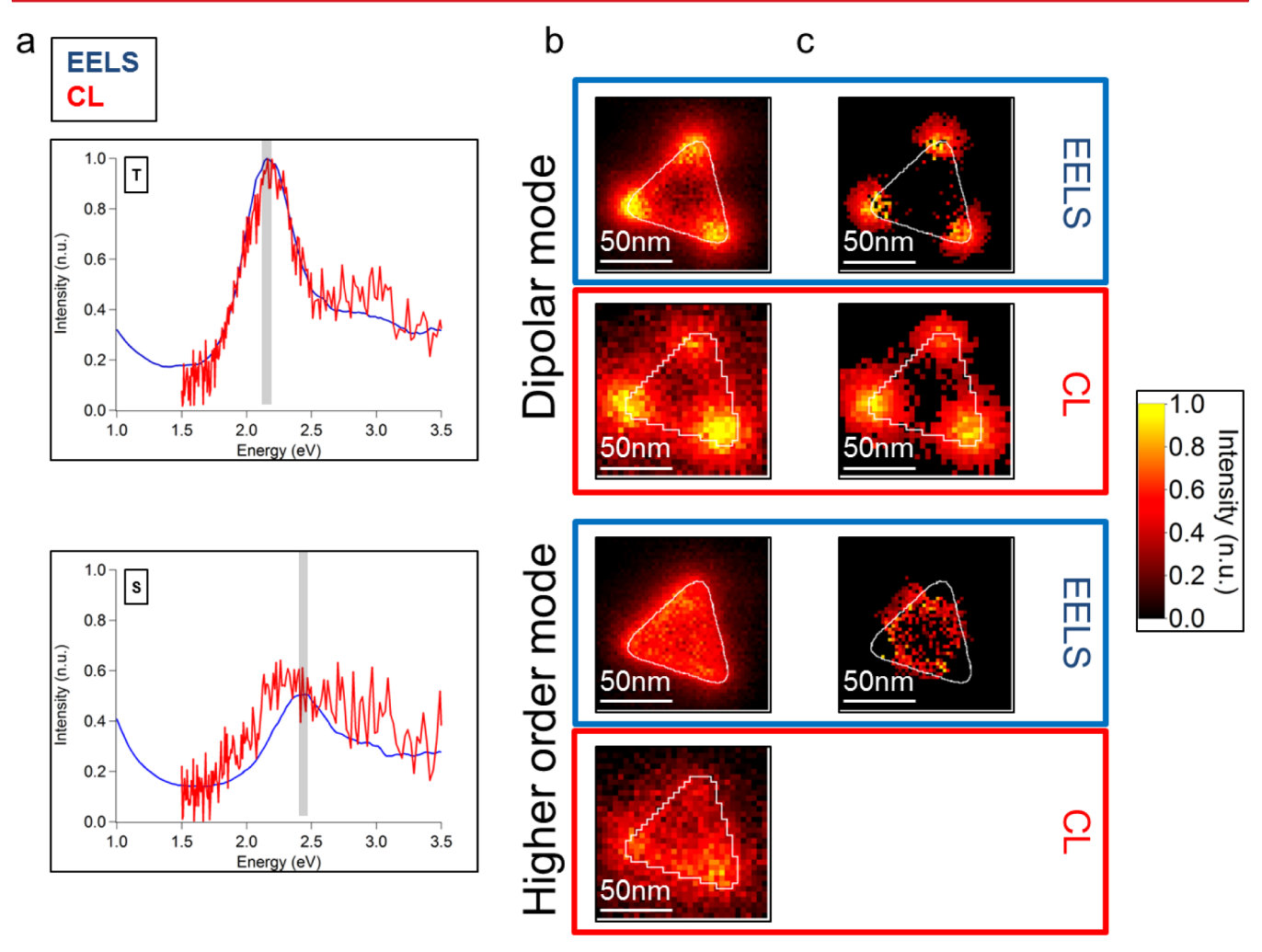


Figure 2. (a) EELS (blue) and CL (red) spectra taken at the low left tip (T) and left side (S) of the 60 nm long, 30 nm thick prism deposited on a graphene sheet shown on Figure 1. The vertical gray windows indicate the spectral ranges considered when building the energy filtered and fitted maps. The spectra are averaged on 9 (EELS) and 25 (CL) pixels of the data sets. (b) EELS and CL maps filtered around the energy of the EELS/CL maxima shown on the T and S panels of (a). (c) Fitted amplitude maps corresponding to the dipolar (EELS and CL) and higher order (EELS only) modes. EELS and CL are independently normalized to their own maxima. The white lines superimposed on the maps indicate the prism shape as obtained from the HAADF image.

the final triangular shape. In this study, two batches of nanoprisms are used. The first one³² consists of monodisperse equilateral 60 nm edge long, 30 nm thick nanoprisms deposited on a graphene sheet. The second one³¹ consists of 80–200 nm edge long (and varying thickness) nanoprisms drop-casted on a thin carbon film. Such nanoparticles are chosen for their high crystallinity, which leads to well-defined resonances both in EELS³³ and CL,³⁴ and because the SP modes that dominate their optical response have been thoroughly discussed in the literature. 20,27,33,35 In particular, in small nanoprisms (such as the 60 nm long ones), the modes are rather simple³⁵ and well described in the quasistatic limit. 20,27 Additionally, the mode energies lie within the experimental range that is accessible with our CL detection system (above 1.2 eV). However, these nanoparticles yield extremely weak CL signals, which might explain why no spatially resolved CL experiments have been previously reported on objects of such a small size.

Experiments are performed using a scanning transmission electron microscope (STEM) fitted with homemade EELS detection⁴ and high efficiency CL detection³⁶ systems, as presented in Figure 1a. Such a microscope generates a subnanometer electron beam that can be scanned over the

region of interest. At each sampling point, a morphological (high angle annular dark field, HAADF) signal is recorded simultaneously with an EELS or a CL spectrum. At the end of the scan, both an HAADF image and a complete set of spatially resolved spectra are collected and can be accurately compared. Alternatively, such a set of spatially resolved spectra can be viewed as a collection of energy filtered maps, which show the spatial distribution of the recorded signal at constant energy (see below for examples). In these experiments, EELS and CL data sets are acquired sequentially because the experimental illumination conditions are drastically different for both spectroscopies, with electron beam currents typically 2 orders of magnitude higher for CL experiments (around 1 nA) than for EELS experiments (around 10-20 pA). Furthermore, typical acquisition times for EELS are 5 to 10 times shorter than for CL. This emphasizes the much higher interaction cross sections when measured by EELS as compared to CL.

As the purpose of the paper is to directly compare both techniques, extreme care is taken in calibrating both spectrometers. Further details can be found in the Methods section. We systematically check that the electron beam does not alter the prisms or the substrate during the scans, and we

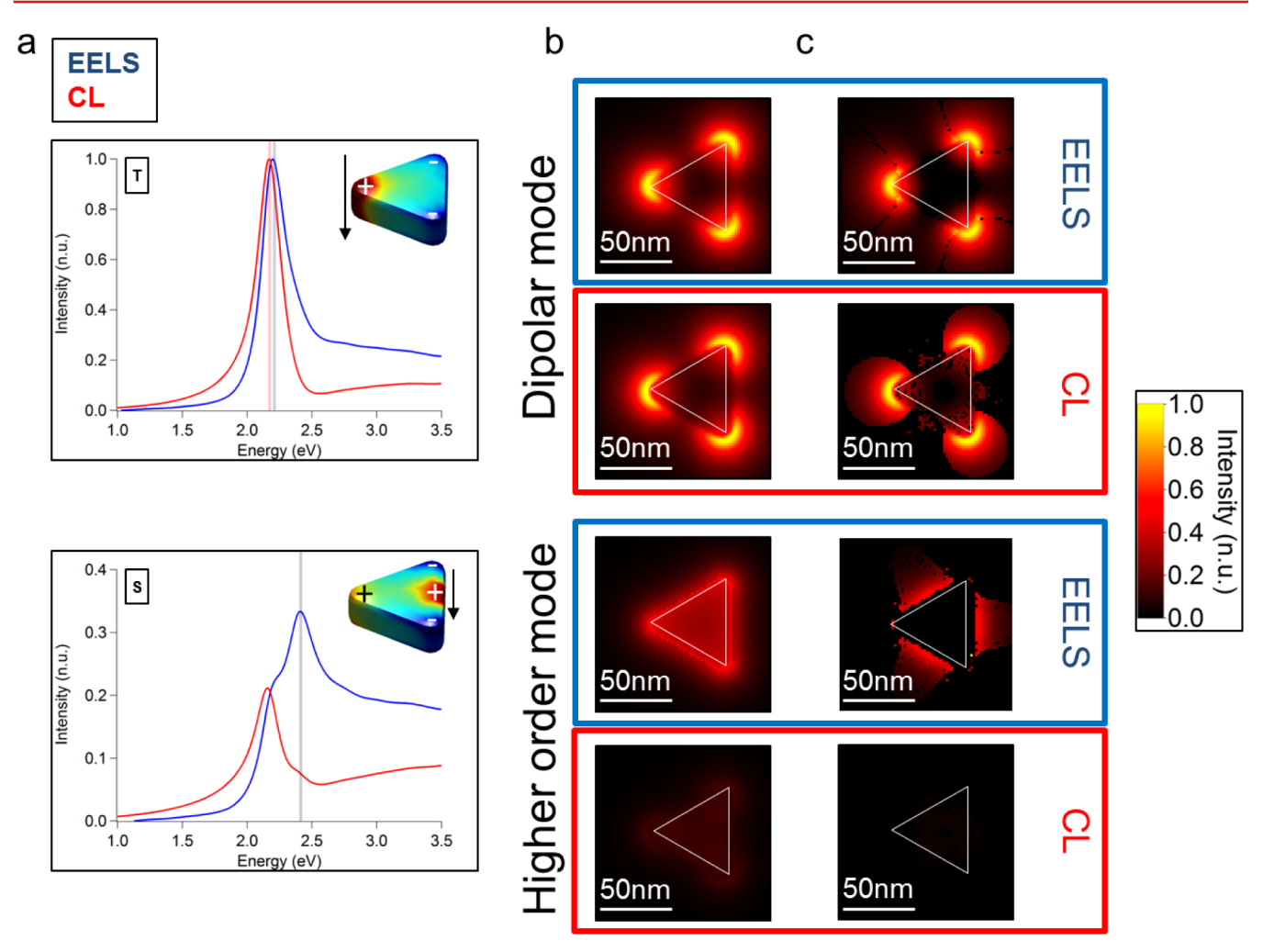


Figure 3. (a) Simulated EELS (blue) and CL (red) spectra calculated at the tip (T) and side (S) of a 60 nm long, 30 nm thick prism surrounded by vacuum. The windows indicate the spectral ranges considered when building the energy filtered and fitted maps of (b) and (c). Inset: surface charges induced by a fast electron beam located at the tip and side (represented as arrows) at the energies of the corresponding EELS maxima. (b) Simulated EELS and CL maps filtered around the energy of the EELS and CL maxima. (c) Simulated fitted amplitude maps corresponding to the dipolar (EELS and CL) and higher order (EELS only) modes. EELS and CL are independently normalized to their own maxima. The white lines superimposed on the maps indicate the prism shape.

discard all experiments in which this happens. We stress that we perform measurements on the very same triangles and environment, thus allowing us to unambiguously compare both physical signals (EELS and CL). This is in stark contrast to previously published CL and EELS measurements performed on related but dissimilar nanoparticles,³⁷ as even slight changes in dimensions or environment can significantly shift energies³⁸ and, thus, impair any quantitative comparison between CL and EELS.

We simulate spatially resolved EELS and CL probabilities, as well as extinction and scattering cross sections, using the retarded boundary-element method (BEM),³⁹ which allows us to account for the particle morphologies³⁷ and, when appropriate, model carbon substrates. The dielectric function of gold and amorphous carbon are taken from optical data.^{40,41} When needed, in order to increase the effect of dissipation, the imaginary part of the dielectric functions are modified as described in ref 23 (see Methods).

As a first illustration, Figure 1b presents the HAADF image and colored maps obtained from spatially resolved EELS and CL experiments performed on a 60 nm-wide triangle lying on a graphene sheet. Total acquisition times for the whole

experiments are 157 s for CL and 16 s for EELS. In the color maps, the color and intensity of each pixel can be related to the energy and amplitude of a locally measured resonance. These maps clearly show that two main excitations, located at the tips (lower energy excitation, yellowish color) and at the sides (higher energy excitation, greenish color) of the nanoprism, are measured in EELS, whereas only the low energy one is observed in CL. It is worth noting that such maps can be generated on the fly right after acquisition without resorting to the more lengthy procedures required for a quantitative analysis described below.

In order to quantitatively analyze the features already suggested by Figure 1b, we show in Figure 2a the EELS (blue) and CL (red) spectra corresponding to an electron probe located at the tip (T) and side (S) of this nanoprism. The filtered maps of Figure 2b display the spatial variations of the EELS (blue framed maps) and CL (red framed maps) signals averaged over two narrow (50 meV wide) energy windows centered on the resonances revealed in the EELS spectra. Beyond such filtered maps, we analyze the SP modes probed by both techniques by processing and fitting each spectrum of the data sets to a sum of Gaussian functions. 43,44

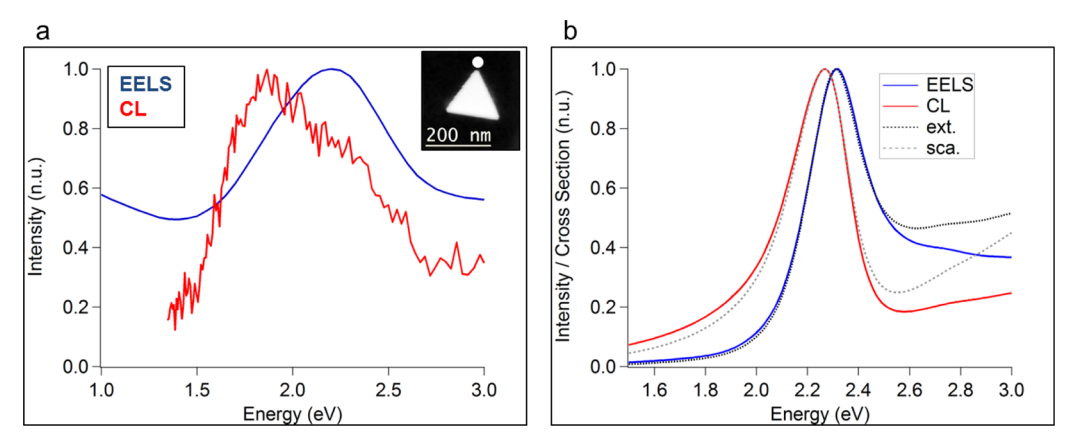


Figure 4. (a) Measured EELS (blue) and CL (red) spectra taken at the tip of a 140 nm edge long gold prism lying on a carbon foil. Inset: HAADF image of the nanoprism. The white disk indicates the electron beam position. (b) Calculated extinction (black dotted line) and scattering spectra (gray dotted line) superimposed to calculated EELS (blue) and CL (red) tip spectra for a single small nanoprism of 50 nm edge length, 50 nm thickness surrounded by vacuum. In the case of the optical cross sections, the light propagation direction is chosen perpendicular to the prism, and the polarization is parallel to one of the edges.

By doing so, each Gaussian peak can be associated with an optical mode. 4,12,23,37,38,43,44 An intensity map of a given mode is then retrieved by assigning to each image pixel the peak amplitude measured in the spectrum that is recorded at the corresponding electron probe position. Such amplitude maps are shown in Figure 2c and correspond to modes resonating at the energies associated with the maxima visible in the EELS and CL spectra. Data analysis based on such fitting techniques allows us to lift the ambiguities generally found in filtered maps, in which the origin of a given intensity change cannot be clearly identified, as it can result from a peak energy change or the tail of a neighboring intense mode (see refs 23 and 24). As already demonstrated, ^{27,35} the two dominant modes that appear in the EELS data correspond to a low-energy dipolar mode, with charge density peaking at the tips, and a higher-energy non dipolar mode, with charge density peaking at the tips and edges (see inset of Figure 3a). The nondipolar mode, loosely denoted here as a higher order mode, has been historically referred to as quadrupolar³⁵ but has been recently recast as hexapolar.²⁰ When averaging over the three tips and sides, we note that these modes are resonant at $E_{\rm EELS}^{\rm d,exp} = 2.16 \pm 0.02$ eV and $E_{\rm EELS}^{\rm ho,exp}$ = 2.41 ± 0.02 eV, respectively. Strikingly, the CL data exhibit just the dipolar mode (resonant at $E_{\rm CL}^{\rm d,exp} = 2.18 \pm 0.02$ eV), as implied by the featureless spectrum and map filtered at the higher order mode energy, which shows only a background intensity without any spatial variations. We also note that the spatial distributions of EELS and CL intensities are similar for the dipolar mode, as suggested by previously reported EELS^{4,27,33} and CL³⁴ separate experiments. These conclusions confirm the above qualitative analysis based in Figure 1b. The darkening of the higher order mode in CL is corroborated by the simulations shown in Figure 3. Considering the absolute energy values, the agreement between simulations and experiments is quite satisfactory without taking into account any substrate. More precisely, they show that the dipolar mode is resonant at $E_{\rm EELS}^{\rm d,sim}$ = 2.20 \pm 0.005 eV in EELS and $E_{\rm CL}^{\rm d,sim}$ = 2.17 \pm 0.005 eV in CL. Furthermore, the higher order mode appears as an additional clear peak at $E_{\rm EELS}^{\rm ho, sim} = 2.41 \pm 0.005$ eV in EELS, whereas it is barely visible in CL. The small energy difference between the EELS and CL dipolar resonances, which lies within the experimental error bars, is discussed in more details further on. Moreover, we note that the full width at half-maximum (fwhm) of the calculated EELS and CL resonances ($\sigma_{\rm EELS}^{
m d,sim}$ =

 $\sigma_{\rm EELS}^{\rm d,sim}=230\pm5$ meV) are in good agreement with those obtained from the CL measurements ($\sigma_{\rm CL}^{\rm d,exp}=245\pm20$ meV) but are slightly smaller than those of the EELS measurements ($\sigma_{\rm EELS}^{\rm d,exp}=260\pm20$ meV). We attribute this effect to the lower experimental energy resolution of EELS as compared with CL. The remarkable agreement between the experimental and calculated CL fwhm, thus, confirms the weak influence of the graphene sheet on the actual measurements. The absence of any higher order mode within the CL data set is a direct experimental demonstration of the drastically different characters of EELS and CL signals, which has been theoretically anticipated for several years. 16,24,25 CL only probes the radiative modes, which are dipolar modes for small objects, while EELS probes all the modes. We note that higher order modes may be radiative for larger triangles leaving the quasistatic regime.

We now focus on a more systematic comparison of EELS and CL measurements of dipolar modes in small nanoprism, before drawing a parallel with optical extinction and scattering. In the case shown in Figures 2 and 3 (small, graphenesupported particles), the dipolar energy positions as measured in EELS and CL are very similar. However, the situation is different when considering larger nanoprisms on carbon films. Although the spatial distributions of EELS and CL intensities are rather similar in both spectroscopies, just as for the smaller triangles, a difference arises for the resonance energies (see e.g., Figure S1 in Supporting Information). Figure 4a shows experimental EELS and CL spectra recorded when the electron probe is located at the tip of a nanoprism lying on a carbon foil. Although associated with the same dipolar mode, the EELS resonance is strikingly blue-shifted with respect to the CL resonance. Also, the fwhm are larger in this case than for the small triangles lying on graphene. Similar shifts and increased broadening are measured repeatedly on nanoprisms lying on a carbon foil, and are reminiscent of extinction and scattering phenomena. Indeed, as a very simple example, Figure 4b shows calculated extinction and scattering spectra superimposed on calculated EELS and CL tip spectra for an individual small nanoprism. The resemblance between EELS (CL) and extinction (scattering) is remarkable around the resonances. In particular, extinction is also blue-shifted with respect to scattering, and the shift is the same as between EELS and CL.

In order to seek a deeper and more intuitive understanding of these observations, we adopt an analytical approach derived

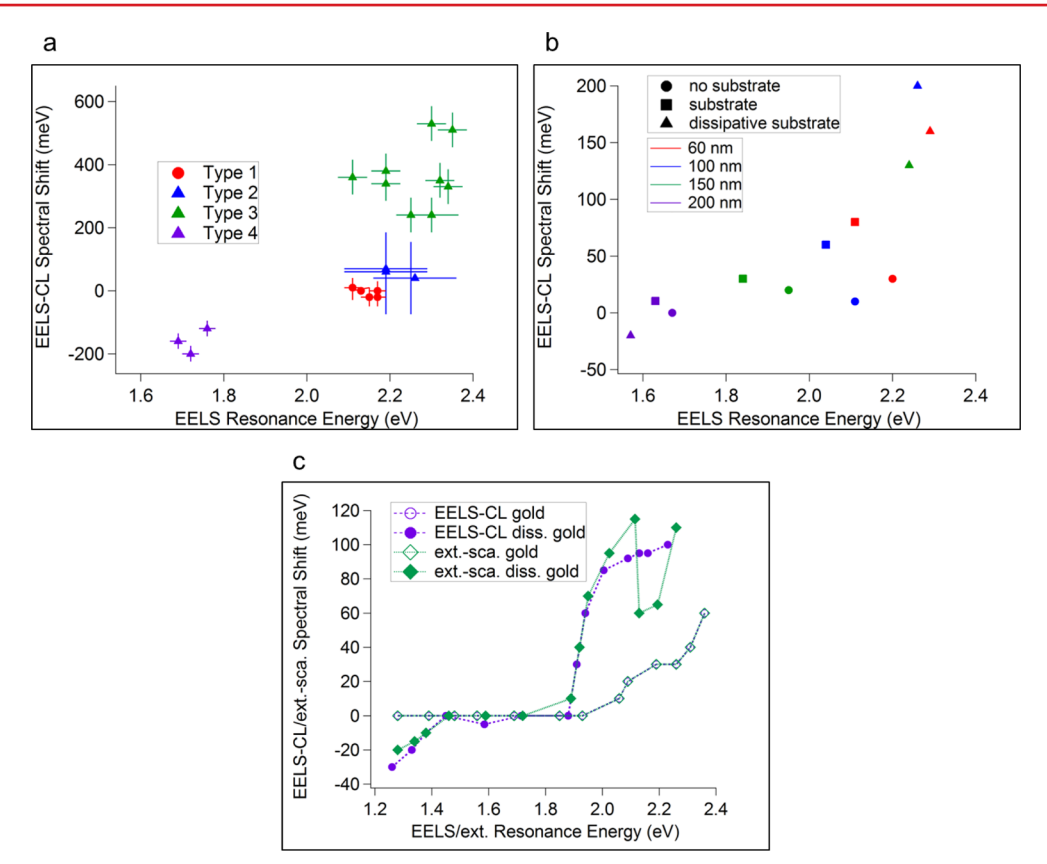


Figure 5. (a) EELS-CL spectral shifts as measured at the tips of several gold nanoprisms. The nanoprisms are color-sorted in four different types. Type 1: small 60 nm edge long nanoprism lying on a graphene sheet. Type 2: 90 nm edge long nanoprism lying on a carbon foil. Type 3: 130–150 nm edge long nanoprisms lying on a carbon foil. Type 4: 160 nm edge long nanoprism lying on a carbon foil. (b) EELS-CL spectral shifts as obtained from tip spectra of gold nanoprisms of various sizes simulated within the retarded BEM framework, with and without sparsely or highly dissipative carbon substrates. The nanoprisms have a constant aspect ratio of 2, and the numbers in the caption correspond to the edge lengths. (c) Spectral shifts between EELS and CL (round purple symbols), and extinction and scattering (diamond green symbols), predicted within the quasistatic modal decomposition model described in the text when using the dielectric function of ref 40. The resonances are calculated for various dipolar modes of gold objects with tabulated dissipation (unfilled symbols) and increased dissipation simulated by multiplying the imaginary part of the tabulated dielectric function by a factor of 5 (filled symbols). The resonance energies are tuned by changing the eigenvalue λ_i (see text). Note that in the case of low dissipation, there is no visible difference between EELS (CL) and extinction (scattering).

from the nonretarded BEM formalism in the quasistatic limit 12,14,15,18,19 (see Supporting Information for a more detailed description and the complete derivation). This formalism enables a direct comparison between the quantities measured by optical and fast electron based spectroscopies through simple analytical expressions. In particular, the absorption and scattering cross sections can be shown to reduce to $C_{\rm abs}(\omega) = \sum_{i=d} A_{i,{\rm abs}} \omega {\rm Im} \{f_i(\omega)\}$ and $C_{\rm sca}(\omega) = \sum_{i=d} A_{i,{\rm sca}} \omega^4 |f_i(\omega)|^2$, where $A_{i,{\rm abs}}$ and $A_{i,{\rm sca}}$ are energy-independent prefactors and

$$f_i(\omega) = \frac{\lambda_i + 1}{\lambda_i - \lambda(\omega)} \tag{1}$$

In this expression, λ_i is a real eigenvalue characterizing mode i, and $\lambda(\omega) = (1 + \varepsilon(\omega))/(1 - \varepsilon(\omega))$ contains the dielectric function of the metallic object $\varepsilon(\omega)$. The physical meanings of the spectral function $f_i(\omega)$ and of λ_i can be found in refs 12, 15, and 24. In the modal decompositions, the sums run over all the dipolar modes of the system. Obviously, the extinction and absorption cross sections are the same, ⁴⁵ as the scattering cross section vanishes in the quasistatic limit. Thus, the physics of extinction is driven by absorption, and we can place extinction and absorption on an equal footing. Furthermore, it has been

shown that the EEL probability at point \vec{R}_{\perp} in a plane perpendicular to the electron beam (along z) reduces to ¹²

$$\Gamma_{\text{EEL}}(\vec{R}_{\perp}, \, \omega) = A_{\text{EEL}} \sum_{i} \operatorname{Im} \{ f_{i}(\omega) \} \left| \tilde{\phi}_{i}(\vec{R}_{\perp}, \, \frac{\omega}{\nu}) \right|^{2}$$
(2)

where A_{EEL} is an energy-independent prefactor and $\tilde{\phi}_i(\vec{R}_\perp,q_z)$ is the Fourier transform of the eigenpotential of mode i $\phi_i(\vec{R}_\perp,z)$ along the beam direction. In a similar way, one can write the CL probability as

$$\Gamma_{\rm CL}(\vec{R}_{\perp}, \omega) \approx \sum_{i=d} A_{i,\rm CL} \omega^3 |f_i(\omega)|^2 \left| \tilde{\phi}_i(\vec{R}_{\perp}, \frac{\omega}{\nu}) \right|^2$$
(3)

where $A_{i,CL}$ is an energy-independent prefactor. In contrast to EELS, the sum only runs over the dipolar modes (i.e., the only ones that contribute to radiation in the small particle limit).

Equations 2 and 3 show that for a given dipolar mode i, the spatial dependences are the same in EELS and CL, as observed experimentally and in the simulations. They have a well-defined physical meaning, given by the spatial modulations of $|\tilde{\phi}_i|\vec{R}_{\perp},\omega/\nu|^2$. Furthermore, the above expressions clearly reveal that the spectral profiles of both EELS and absorption/extinction are proportional to the same spectral function $\mathrm{Im}\{f_i(\omega)\}$. Likewise,

CL and scattering are both proportional to $|f_i(\omega)|^2$. This finding constitutes a generalization to an arbitrary shape of a well-known result in the special case of a small sphere 16,24,45 and explains in simple terms why EELS and extinction on the one hand and CL and scattering on the other are so closely related. Indeed, although both the square modulus and imaginary parts of $f_i(\omega)$ have the exact same maximum energies in the absence of dissipation, they shift when dissipation is present. For instance, by inserting a Drude model expression $\varepsilon(\omega) = 1 - \omega_p^2/(\omega^2 + i\Gamma\omega)$ (ω_p being the bulk plasmon energy and Γ a damping term) into eq 1, one finds the following Lorentziantype expressions for the imaginary part and square modulus of $f_i(\omega)$

$$\operatorname{Im}\{f_{i}(\omega)\} = \frac{\Gamma \tilde{\omega}_{i}^{2} \omega}{\Gamma^{2} \omega^{2} + (\omega^{2} - \tilde{\omega}_{i}^{2})^{2}}$$
(4)

$$|f_i(\omega)|^2 = \frac{\tilde{\omega}_i^4}{\Gamma^2 \omega^2 + (\omega^2 - \tilde{\omega}_i^2)^2}$$
(5)

where $\tilde{\omega}_i = \sqrt{1 + \lambda_i} \omega_p / \sqrt{2}$ is the well-known nondissipative SP energy, which has a simple dependence on λ_i in the Drude model. Because with this analytical dielectric constant Im- $\{f_i(\omega)\} \propto \omega |f_i(\omega)|^2$, it is clear that these two quantities do not have the same resonance energies. This is consistent with the observation that the maximum oscillation amplitude of a driven harmonic damped oscillator (which corresponds to the maximum dipole moment and, thus, can be connected to the light emission induced either by light or fast electrons) occurs at a lower frequency that the maximum energy transfer. 46 Such effect has been invoked to explain the spectral shifts between near-field probe and far-field spectra⁴⁷ and has already been reported theoretically for extinction and scattering.⁴⁸ These expressions also predict that the magnitude of the shift increases with the amount of dissipation, which is in agreement with the fact that a shift is measured between EELS and CL only on large particles lying on a carbon foil.

As a further investigation of such spectral shifts, Figure 5a shows the magnitude of the EELS-CL shifts as measured on different particles. We sort these particles into four different groups: very small particles (60 nm edge long) lying on a graphene sheet (type 1), and larger particles of various sizes (90 nm, 130-150 nm, and 160 nm edge long) lying on a carbon foil (types 2, 3, and 4, respectively). We can speculate two different reasons to explain the shifts: large particle sizes and absorbing substrate. Thus, we perform additional retarded BEM simulations for gold nanoprisms with different sizes, with and without sparsely or highly dissipative carbon substrates (see Methods). For simplicity, we keep a constant aspect ratio of 2 and vary the edge length. The output is summarized in Figure 5b. For a given size, the substrate either induces or increases the spectral shift between EELS and CL by an amount related to its dissipating influence, in accordance with the quasistatic theory. We stress that the exact energy positions and shifts depend both on the size of the object and the absorption properties of the substrate, which makes any truly quantitative comparison between experiments and simulations extremely difficult. In particular, the thickness of most of the objects, as well as the exact dielectric properties of the substrate and environment, are unknown. As a matter of fact, the magnitude of the shift is always much larger in experiments than in simulations, which we tentatively attribute to an underestimate of dissipation. However, it is striking that the calculated trend is in qualitative

agreement with the experiment (compare Figure 5a and b). Interestingly, this trend cannot be captured by our model when describing the metal with a simple Drude model. In particular, taking into account the right energy dependent prefactors of the modal decompositions, egs 4 and 5 imply that a dipolar mode would induce a CL (scattering) resonance blue-shifted relative to its corresponding EELS (extinction) resonance, which is contrary to what is observed in most of the cases. Nevertheless, the complete trend is qualitatively recovered by the model, not only for EELS and CL but also for extinction and scattering, when introducing tabulated gold dielectric function⁴⁰ into eq 1 (see Figure 5c). This points out the importance of taking into account interband transitions in gold in this energy range to accurately describe the difference between absorption and scattering phenomena. This trend can be summarized as follows: the shift between EELS/extinction and CL/scattering, whose magnitude increases with the dissipation level, is increasingly negative below typically 1.6 eV, where gold behaves as a good Drude metal, and is increasingly positive above 1.8 eV, where it is dominated by its interband transitions. 49 The quasistatic modal decompositions are thus capable of generally explaining the close similarities between EELS and extinction shown in recent experiments⁵⁰ and call for an experimental comparison of CL and scattering to confirm their predicted resemblance.

In conclusion, we report spatially resolved EELS and CL measurements on the very same gold nanoprisms. They lead to the possibility of directly sorting out radiative and nonradiative modes. We show that a radiative mode, depending on the size and substrate, may be clearly observable at different resonance energies in both EELS and CL. These results are in agreement with fully retarded BEM electromagnetic simulations, which also indicate that such spectral differences originate in dissipation and are similar to those observed between optical extinction and scattering. These observations are explained using a modal decomposition analysis, which allows us to link the macroscopic concepts of extinction and scattering to spatially resolved EELS and CL experiments. We expect that these conclusions can be extrapolated to larger particles, for which similar retarded modal decompositions are needed to deal with more delocalized SP modes. We further hope that the present work sheds some light on the experimental retrieval of spectral and spatial information on plasmons.

Methods. The experiments are performed using a Vacuum Generator HB-501 scanning transmission electron microscope (STEM) equipped with a cold field emission electron gun. Both CL and EELS measurements are carried out at an operation voltage of 100 kV. The incident electron beam semiangle for EELS is set to 7.5 mrad, resulting in typical currents of 10-20 pA for a probe size of 0.7 nm. The incident semiangle for CL is set to 15 mrad, resulting in currents of more than 1 nA and a probe size of a few nanometres. The collection semiangle is 9 mrad for EELS, whereas the solid detection angle is $1.2~\pi$ sterad for CL.

Small monodisperse and larger nanoprisms are measured. The larger nanoprisms are dropcasted on a standard TEM grid, whereas the small ones are dropcasted on graphene sheets (Ted Pella Single Layer Graphene). The thickness of the monodisperse nanoprisms is monitored by deliberately damaging the graphene sheet by extreme illumination conditions. This leads to the deterioration of the sheet and the subsequent tilt of the nanoprism.

The dispersion of the electron and optical spectrometers are carefully measured through different calibration procedures. The EELS calibration is performed by applying a 10 V voltage difference on the drift tube and measuring the resulting spectral shift of the zero loss peak (ZLP) of an averaged spectrum recorded in vacuum (vacuum ZLP). The CL calibration is performed by systematically recording an Hg lamp emission spectrum after the experiments.

After acquisition, the EELS spectra are spectrally aligned and binned together. The resulting set of spectra is then deconvolved by the vacuum ZLP through Richardson Lucy deconvolution. The dark noise of the CCD camera together with a very small signal contribution coming from the substrate are removed from the CL spectra by averaging and subtracting a few spectra recorded from the substrate.

After deconvolution, the spectral resolution for EELS, as estimated from the fwhm of the deconvolved vacuum ZLP, is of the order of 150 meV. The spectral resolution for CL is of the order of 30 meV, as estimated from the fwhm of the emission lines of the Hg lamp.

The EELS and CL local spectra shown on this article are averaged over a few pixels around the locations shown on the images. They are fitted to a single Gaussian function plus a sigmoid background to precisely access the resonance energies. All along this article, the errors given for each resonance include the calibration error as well as a possible fitting error. When the resonance energies and peak fwhm associated with the dipolar and higher order modes are discussed, the values also take into account an average over the resonances as measured at the three tips and sides of the nanoprism. In order to build maps such as the ones used in Figures 1 and 2, all the EELS spectra contained in the spatially resolved data set are first normalized and subtracted from the ZLP.4 Prior to fitting, the noise of the CL spectra is reduced via principal component analysis. 52 Multipeak fitting is performed on both EELS and CL data sets using a sum of Gaussian functions and a sigmoid background within each spectrum.³⁸ Maps of the amplitude of those peaks whose central energy is found within a given energy range are produced by assigning to each probe position the amplitude of the Gaussian function that is fitted within the corresponding spectrum in this energy range. For all the maps shown in this paper, we make sure that only one fitted Gaussian function has its center in the selected, narrow energy range.

The boundary element method (BEM) numerical simulations are achieved using either BEM-3D³⁷ or the MNPBEM toolbox⁵³ with its EELS/CL extension,⁵⁴ with the CL spectra computed as described in ref 55. Simulations including a substrate are performed by adding a 5 nm thin cylinder upon which the nanoprism stands completely. To account for additional dissipation of the substrate, we arbitrarily multiply the imaginary part of the dielectric function of amorphous carbon⁴¹ by 2. The amplitude maps of Figure 3c are obtained by calculating complete EELS and CL spectra at different probe positions and applying the same fitting procedure as for the experiment.

ASSOCIATED CONTENT

S Supporting Information

Further experiments, theoretical derivations and detailed interpretations are provided in Supporting Information. This material is available free of charge via the Internet at http://pubs.acs.org/.

AUTHOR INFORMATION

Corresponding Author

*E-mail: kociak@lps.u-psud.fr.

Notes

The authors declare no competing financial interest.

ACKNOWLEDGMENTS

This work has received support from the French State managed by the National Agency for Research under the program of future investment EQUIPEX TEMPOS-CHROMATEM with the reference ANR-10-EQPX-50, the HYNNA project, as well as the French General Directorate for Armament. The research leading to these results has received funding from the European Union Seventh Framework Programme [No. FP7/2007-2013] under Grant Agreement No. n312483 (ESTEEM2). L.F.Z. acknowledges funding form the São Paulo Research Foundation (FAPESP), grants 2011/05989-5 and 2013/06167-4. V.M. acknowledges financial support through JAE from CSIC. L.M.L.-M. acknowledges funding from the European Research Council Advanced Grant PLASMAQUO (No. 267867). M.K. and A.L. want to thank S. Meuret for help in designing test samples not presented in this study and U. Hohenester for advice in setting substrate simulations using the MNPBEM toolbox. The authors also appreciate financial support from the European Union under the Seventh Framework Program (Integrated Infrastructure Initiative N. 262348 European Soft Matter Infrastructure, ESMI).

■ REFERENCES

- (1) Batson, P. Phys. Rev. Lett. 1982, 49, 936-940.
- (2) Weeber, J.-C.; Dereux, A.; Girard, C.; Krenn, J. R.; Goudonnet, J.-P. *Phys. Rev. B* **1999**, *60*, 9061–9068.
- (3) Yamamoto, N.; Araya, K.; García de Abajo, F. J. Phys. Rev. B 2001, 6420, 205419.
- (4) Nelayah, J.; Kociak, M.; Stéphan, O.; García de Abajo, F. J.; Tence, M.; Henrard, L.; Taverna, D.; Pastoriza-Santos, I.; Liz-Marzán, L. M.; Colliex, C. *Nat. Phys.* **2007**, *3*, 348–353.
- (5) Bosman, M.; Keast, V. J.; Watanabe, M.; Maaroof, A. I.; Cortie, M. B. Nanotechnology 2007, 18, 165505.
- (6) Vesseur, E. J. R.; de Waele, R.; Kuttge, M.; Polman, A. Nano Lett. **2007**, 7, 2843–2846.
- (7) Douillard, L.; Charra, F.; Korczak, Z.; Bachelot, R.; Kostcheev, S.; Lerondel, G.; Adam, P. M.; Royer, P. *Nano Lett.* **2008**, *8*, 935–940.
- (8) Rossouw, D.; Couillard, M.; Vickery, J.; Kumacheva, E.; Botton, G. A. Nano Lett. 2011, 11, 1499–1504.
- (9) Joulain, K.; Carminati, R.; Mulet, J. P.; Greffet, J. J. Phys. Rev. B 2003, 68, 245405.
- (10) Stockman, M.; Faleev, S.; Bergman, D. Phys. Rev. Lett. 2001, 87, 167401.
- (11) Dereux, A.; Girard, C.; Weeber, J. C. J. Chem. Phys. 2000, 112, 7775-7789.
- (12) Boudarham, G.; Kociak, M. Phys. Rev. B 2012, 85, 245447.
- (13) De Wilde, Y.; Formanek, F.; Carminati, R.; Gralak, B.; Lemoine, P. A.; Joulain, K.; Mulet, J. P.; Chen, Y.; Greffet, J. J. *Nature* **2006**, *444*, 740–743.
- (14) Ouyang, F.; Isaacson, M. Philos. Mag. B 1989, 60, 481-492.
- (15) García de Abajo, F. J.; Aizpurua, J. Phys. Rev. B **1997**, 56, 15873–15884.
- (16) García de Abajo, F. J. Phys. Rev. B 1999, 59, 3095-3107.
- (17) García de Abajo, F. J.; Kociak, M. Phys. Rev. Lett. 2008, 100, 106804.
- (18) Hohenester, U.; Ditlbacher, H.; Krenn, J. R. Phys. Rev. Lett. 2009, 103, 106801.
- (19) Hörl, A.; Trügler, A.; Hohenester, U. Phys. Rev. Lett. 2013, 111, 076801.

(20) Schmidt, F. P.; Ditlbacher, H.; Hofer, F.; Krenn, J. R.; Hohenester, U. *Nano Lett.* **2014**, *14*, 4810–4815.

- (21) Vesseur, E. J. R.; García de Abajo, F. J.; Polman, A. Nano Lett. **2009**, *9*, 3147–3150.
- (22) Kuttge, M.; Vesseur, E. J. R.; Koenderink, A. F.; Lezec, H. J.; Atwater, H. A.; García de Abajo, F. J.; Polman, A. *Phys. Rev. B* **2009**, 79, 113405.
- (23) Losquin, A.; Camelio, S.; Rossouw, D.; Besbes, M.; Pailloux, F.; Babonneau, D.; Botton, G. A.; Greffet, J.-J.; Stéphan, O.; Kociak, M. *Phys. Rev. B* **2013**, *88*, 115427.
- (24) Kociak, M.; Stephan, O. Chem. Soc. Rev. 2014, 43, 3865-3883.
- (25) García de Abajo, F. J. Rev. Mod. Phys. 2010, 82, 209-275.
- (26) Gomez-Medina, R.; Yamamoto, N.; Nakano, M.; García de Abajo, F. J. New J. Phys. 2008, 10, 105009.
- (27) Nelayah, J.; Kociak, M.; Stéphan, O.; Geuquet, N.; Henrard, L.; García de Abajo, F. J.; Pastoriza-Santos, I.; Liz-Marzan, L. M.; Colliex, C. *Nano Lett.* **2010**, *10*, 902–907.
- (28) Bigelow, N. W.; Vaschillo, A.; Camden, J. P.; Masiello, D. J. ACS Nano 2013, 7, 4511–4519.
- (29) Collins, S. M.; Midgley, P. A. Phys. Rev. B 2013, 87, 235432.
- (30) Collins, S. M.; Nicoletti, O.; Rossouw, D.; Ostasevicius, T.; Midgley, P. A. *Phys. Rev. B* **2014**, *90*, 155419.
- (31) Sanchez-Iglesias, A.; Pastoriza-Santos, I.; Perez-Juste, J.; Rodriguez Gonzalez, B.; Garcia de Abajo, F. J.; Liz-Marzan, L. M. Adv. Mater. 2006, 18, 2529–2534.
- (32) Scarabelli, L.; Coronado-Puchau, M.; Giner-Casares, J. J.; Langer, J.; Liz-Marzán, L. M. ACS Nano 2014, 8, 5833–5842.
- (33) Gu, L.; Sigle, W.; Koch, C. T.; Ogut, B.; van Aken, P. A.; Talebi, N.; Vogelgesang, R.; Mu, J. L.; Wen, X. G.; Mao, J. *Phys. Rev. B* **2011**, 83, 195433.
- (34) Das, P.; Chini, T. K.; Pond, J. J. Phys. Chem. C 2012, 116, 5610–15619.
- (35) Hao, E.; Schatz, G. C. J. Chem. Phys. 2004, 120, 357-366.
- (36) Zagonel, L. F.; Mazzucco, S.; Tencé, M.; March, K.; Bernard, R.; Laslier, B.; Jacopin, G.; Tchernycheva, M.; Rigutti, L.; Julien, F. H.; Songmuang, R.; Kociak, M. *Nano Lett.* **2011**, *11*, 568–573.
- (37) Myroshnychenko, V.; Nelayah, J.; Adamo, G.; Geuquet, N.; Rodriguez-Fernandez, J.; Pastoriza-Santos, I.; MacDonald, K. F.; Henrard, L.; Liz-Marzan, L. M.; Zheludev, N. I.; Kociak, M.; García de Abajo, F. J. *Nano Lett.* **2012**, *12*, 4172–4180.
- (38) Mazzucco, S.; Geuquet, N.; Ye, J.; Stéphan, O.; Van Roy, W.; Van Dorpe, P.; Henrard, L.; Kociak, M. *Nano Lett.* **2012**, *12*, 1288–1294.
- (39) García de Abajo, F. J.; Howie, A. Phys. Rev. B 2002, 65, 115418.
- (40) Johnson, B.; Christy, R. W. Phys. Rev. B 1972, 6, 4370-4379.
- (41) Hagemann, H.-J.; Gudat, W.; Kunz, C. *J. Opt. Soc. Am.* **1975**, 65, 742–744.
- (42) Bosman, M.; Anstis, G. R.; Keast, V. J.; Clarke, J. D.; Cortie, M. B. ACS Nano **2012**, *6*, 319–326.
- (43) Mazzucco, S.; Stephan, O.; Colliex, C.; Pastoriza-Santos, I.; Liz-Marzan, L. M.; García de Abajo, F. J.; Kociak, M. Eur. Phys. J.: Appl. Phys. 2011, 54, 33512.
- (44) Bosman, M.; Ye, E.; Tan, S. F.; Nijhuis, C. A.; Yang, J. K. W.; Marty, R.; Mlayah, A.; Arbouet, A.; Girard, C.; Han, M.-Y. Sci. Rep. 2013, 3, 1312.
- (45) Bohren, C. F.; Huffman, D. R. Absorption and scattering of light by small particles; Wiley: New York, 1983.
- (46) Zuloaga, J.; Nordlander, P. Nano Lett. 2011, 11, 1280-1283.
- (47) Alonso-González, P.; Albella, P.; Neubrech, F.; Huck, C.; Chen, J.; Golmar, F.; Casanova, F.; Hueso, L. E.; Pucci, A.; Aizpurua, J.; Hillenbrand, R. *Phys. Rev. Lett.* **2013**, *110*, 203902.
- (48) Kats, M. A.; Yu, N.; Genevet, P.; Gaburro, Z.; Capasso, F. Opt. Express 2011, 19, 21748–21753.
- (49) Etchegoin, P. G.; Le Ru, E. C.; Meyer, M. J. Chem. Phys. 2006, 125, 164705.
- (50) Husnik, M.; von Cube, F.; Irsen, S.; Linden, S.; Niegemann, J.; Busch, K.; Wegener, M. *Nanophotonics* **2013**, *2*, 241–245.
- (51) Gloter, A.; Douiri, A.; Tence, M.; Colliex, C. *Ultramicroscopy* **2003**, 96, 385–400.

- (52) Edwards, P. R.; Sleith, D.; Wark, A. W.; Martin, R. W. J. Phys. Chem. C 2011, 115, 14031–14035.
- (53) Hohenester, U.; Trugler, A. Comput. Phys. Commun. 2012, 183, 370-381.
- (54) Hohenester, U. Comput. Phys. Commun. 2014, 185, 1177-1187.
- (55) Martin, J.; Kociak, M.; Mahfoud, Z.; Proust, J.; Gérard, D.; Plain, J. Nano Lett. **2014**, *14*, 5517–5523.